Materials Advances

Accepted Manuscript

This article can be cited before page numbers have been issued, to do this please use: F. Zannat, Md. A. Alam, P. Ghosh, R. K. Bishwas and S. A. Jahan, *Mater. Adv.*, 2025, DOI: 10.1039/D5MA01083G.

ROYAL SOCIETY OF CHEMISTRY

rsc.li/materials-advances

View Article Online
DOI: 10.1039/D5MA01083G

Sustainable Synthesis of α-Alumina Nanoparticles: Comparative Study of Base-Mediated Crystallization via Co Precipitation

Fariha Zannat[a], Md. Ashraful Alam[a], Pulak Ghosh[b], Raton Kumar Bishwas[a*], Shirin Akter Jahan[a*]

[a] Institute of Glass and Ceramic Research and Testing (IGCRT), Bangladesh Council of Scientific and Industrial Research (BCSIR), Dhaka-1205, Bangladesh

[b] Department of Chemistry, Govt. Tolaram College, Narayanganj, Narayanganj-1400, Bangladesh

Corresponding author: Raton Kumar Bishwas; rk_bishwas@bcsir.gov.bd & Shirin Akter Jahan; shirin_akter@bcsir.gov.bd

Abstract

Alpha-alumina (α-Al_2O_3) nanoparticles (NPs) were synthesized via a controlled co-precipitation method using three different bases: sodium hydroxide (NaOH), potassium hydroxide (KOH), and ammonium hydroxide (NH_4OH). The influence of each base on the structural, optical, and surface properties of the synthesized nanoparticles was systematically investigated. Characterization techniques, including powder X-ray diffraction (PXRD), dynamic light scattering (DLS), UV-Vis spectroscopy, and zeta potential analysis, were employed. Crystallite size, estimated using multiple models, ranged from 54.67 nm to 94.74 nm, with NH_4OH yielding the smallest size and highest specific surface area (28.36 m^2/g). Rietveld refinement confirmed complete α-phase formation for the NaOH and NH_4OH samples, while the KOH-derived sample exhibited minor potassium oxide impurities. UV-Vis analysis revealed a wide band gap (5.4-5.5 eV), and zeta potential measurements indicated enhanced colloidal stability for samples synthesized using NaOH and NH_4OH. Thermogravimetric and differential scanning calorimetry confirmed α-phase development between 1047-1121°C. Transmission electron microscopy revealed spherical morphology and nanoscale particle size. These findings highlight the critical role of base selection in tuning the physicochemical properties of α-alumina and demonstrate the effectiveness of

View Article Online
DOI: 10.1039/D5MA01083G

NH_4OH in producing fine, phase-pure, and stable α-Al_2O_3 nanoparticles suitable for applications in high-temperature ceramics, electronics, and photocatalysis.

Keywords: α-alumina, Nanoparticles, Co-precipitation, X-ray diffraction, WPPF.

View Article Online
DOI: 10.1039/D5MA01083G

1. Introduction

Alumina (Al_2O_3) is a crucial oxide extensively utilized in ceramics, electrical engineering, and petrochemical sectors [1][2]. Among its polymorphic forms, the alpha phase (α-Al_2O_3), also known as corundum, is particularly valued for its superior thermal stability, high hardness, chemical inertness, and electrical insulating properties [4][5][6]. These features make α-alumina a critical material in a broad range of industries, including electronics, catalysis, protective coatings, and structural ceramics [7][8]. The α-phase is the most stable crystallographic form of alumina, especially at elevated temperatures, and exhibits a hexagonal close-packed structure [9]. Typically, the formation of α-alumina requires calcination at temperatures above 1100 °C, during which metastable transitional phases such as γ-, δ-, or θ-alumina may form and gradually convert to the α-phase [10]. Therefore, the control of synthesis parameters is essential for obtaining pure α-phase alumina nanoparticles with desirable properties [11]. Among the various synthesis techniques developed to produce alumina nanoparticles, such as sol gel [12], hydrothermal [13], and combustion methods [14], the co-precipitation approach stands out for its simplicity, scalability, and low production cost [15][16]. This method enables precise control of stoichiometry, particle morphology, and size distribution by adjusting key process parameters [17]. Notably, the nature of the base used during precipitation plays a significant role in influencing the nucleation rate, crystallinity, and final morphology of the product. Different bases introduce varying ionic environments that can affect the hydrolysis and condensation kinetics of the aluminum precursor [18]. Previous studies have typically focused on individual bases, leaving limited comparative insight into how different hydroxides systematically affect crystallite size, morphology, phase stability, and colloidal performance.

This study offers a systematic and comparative evaluation of how different alkaline bases, NaOH, KOH, and NH_4OH, influence the physicochemical characteristics of α-alumina NPs synthesized by co-precipitation. Unlike previous studies that focused on a single base, this work employs X-ray diffraction along with thermal analysis, optical analysis, morphological observation, and particle size measurements to comprehensively investigate the influence of different bases on the material. The findings offer a practical pathway to tailor nanoparticle properties for advanced ceramic, catalytic, and electronic applications, and highlight ammonium hydroxide as a superior base for producing fine, stable, and phase-pure α-alumina NPs.

View Article Online
DOI: 10.1039/D5MA01083G

2. Materials and Methods

2..1 Materials

The chemicals employed in this study included Aluminum nitrate nonahydrate [Al $(NO_3)_3.9H_2O$, 99.60%, Merck, Germany], Methanol [99.90%, Merck, Germany], Sodium hydroxide, Potassium hydroxide, Ammonium hydroxide solution (NH_4OH) [25.0%, Merck, Germany] and deionized (DI) water utilized throughout the experimental procedures. The DI water was sourced from the deionized water plant, Inorganic Pigment and Chemical Research Division (IPCRD), IGCRT plant of BCSIR, Bangladesh.

2.2. Synthesis Route of Alumina

5.0 grams of $Al(NO_3)_3 \cdot 9H_2O$ were precisely weighed [ATY224, Shimadzu, Japan] and solubilized in 100.0 mL of deionized (DI) water. The mixture was subjected to continuous stirring [UC 152, Stuart, USA] at ambient temperature for 30.0 minutes to ensure total solubility of the component. Then base solution was slowly added to the solution until the pH was precisely adjusted to 9.0, monitored using a pH meter (STARTER 3100, OHAUS, China). The mixture was further stirred for 30.0 minutes, then allowed to stand for 12.0 hours to ensure complete settling of the precipitate. The obtained precipitate was repeatedly washed three times with DI water and three times with ethanol to eliminate ions and any remaining water and ethanol-soluble impurities. The precipitate was then dried at 110.0 °C for 12.0 hours in an oven (ED115, BINDER, USA) to ensure the complete removal of moisture and volatile organics. Finally, the dried powder was finely crushed using a mortar and then calcined in a muffle furnace (LHTC 08/16, Nabertherm, Germany) at 1200.0 °C for 4.0 hours in air, employing a controlled heating rate of 5.0 °C/min to synthesize α-Al_2O_3 powders. The procedure was repeated under identical conditions, with variation in the base used for the pH adjustment, specifically: (A) sodium hydroxide, (B) potassium hydroxide, and (C) ammonium hydroxide, each at a concentration of 0.01 M.

3. Characterization

3.1.1. Crystallographic analysis

Powder X-ray diffraction (PXRD) was employed to characterize the crystallinity and crystal structure of the synthesized α-alumina NPs [19][20][21]. Using X-rays and periodic atom alignments with materials that have a consistent crystalline nanostructure, PXRD is a non-

View Article Online
DOI: 10.1039/D5MA01083G

destructive analysis technique. By exposing the powdered sample of α-alumina NPs to an intense single wavelength X-ray beam, the methodology collected XRD data. Additionally investigated by PXRD were the crystallographic structure, shape, average size, d-spacing, dislocation density, and lattice parameters. In SmartLab SE [Rigaku, Japan], the copper cathode tube receives 50.0 mA× 40.0 kV as the X-ray's power source. Under standard operation mode (SOM), a one-dimensional scan was executed with a scanning speed of 5°/min, employing a step size of 0.01° and a standard detector head. The analysis was carried out within a 2θ angular range of 5.0° to 90.0°, employing an incident slit width of 0.5° and a length limiting slit of 10 mm to ensure precise beam definition. The whole powder pattern fitting (WPPF) method, utilized for quantitative analysis with the ICDD *PDF5+* standard and crystal symmetry, was explored by VESTA software. The Scherrer equation [22] was employed for crystallite size calculation by PXRD. The Scherrer equation typically yields a smaller crystallite size than the actual value, since it attributes diffraction peak broadening solely to finite crystallite dimensions. In practice, additional contributions from lattice strain, structural defects, and other microstructural factors also broaden the peaks, which leads to an underestimation of the true crystallite size [23].

$$D = \frac{K\lambda}{\beta cos\theta} \quad (1)$$

Here, crystallite size is presented as D, λ is the wavelength of the X-ray source (Cu tube; λ= 0.1541 nm), *K* is the crystallite-shape factor (k=0.9), β is the full width at half maximum, and θ is the diffraction angle or Bragg angle. The interplanar distance between the atoms in a crystal system is expressed as the d-spacing values that were determined employing Bragg's law [24].

$$d = \frac{n\lambda}{2sin\theta} \quad (2)$$

Crystallographic analysis of the synthesized NPs included the evaluation of lattice parameters, microstrain, relative intensity, dislocation density, unit cell volume, packing efficiency, preferred growth orientation, specific surface area, and crystallinity index. These parameters were calculated using Eqs. (3) to (12) as presented below.

Lattice parameter for hexagonal crystal structure, $\frac{1}{d^2} = \frac{4}{3}\left\{\frac{h^2+hk+k^2}{a^2}\right\} + \left(\frac{l^2}{c^2}\right)$ (3)

Micro-strain, $\varepsilon = \frac{\beta}{4\,tan\theta}$ (4)

Dislocation density, $\delta = \frac{1}{(D)^2}$ (5)

Specific surface area, $S = \frac{6\times10^3}{\rho\times D}$ (6)

View Article Online
DOI: 10.1039/D5MA01083G

Volume of hexagonal unit cell, $V = a^2c$ (7)

Crystallinity index, CI $= \frac{H_{101}+H_{004}+H_{200}}{H_{101}}$ (8)

Relative intensity, RI $= \frac{Intensity\ of\ a\ certain\ plane,\ I_c}{Intensity\ of\ any\ three\ planes,\ (I_1+I_2+I_3)}$

(9)

Preference growth, P $= \frac{RI_{sample}-RI_{standard}}{RI_{standard}}$ (10)

Atomic packing factor (APF) $= \left(\frac{N_{Al}V_{Al}+N_oV_o}{a^2C}\right)$ (11)

Crystallinity (%) $= \frac{I_{101}}{I_{101}+I_{004}+I_{200}} \times 100$ (12)

The letter H signifies the plane's height, I denotes the plane's peak intensity, "a" and "c" are the lattice parameters of the tetragonal unit cell and h k l correspond to the Miller indices.

3.2. Evaluation of Crystallite Size Through Various Models

Several techniques, including the Scherrer equation, Williamson-Hall plot, Monshi-Scherrer method, and size strain plot model, Shahadat-Scherrer model, and Linear Straight-Line model, were applied to evaluate the crystallite size of the NPs.

3.2.1. Williamson-Hall plot

The Williamson-Hall plot is used to investigate how crystal size and microstrain contribute to broadening peaks observed in X-ray diffraction patterns [25].

$\beta_{total}Cos\theta = \frac{k\lambda}{D} + 4.\varepsilon sin\theta$ (13)

By relating Eq. (13) to the typical linear equation $(y = mx + c)$ we acquired the crystallite size. By plotting $\beta_{total}Cos\theta$ on the Y-axis and $4sin\theta$ on the X-axis, a straight line is constructed. The intercept provides a means to calculate the crystallite size.

3.2.2. Monshi-Scherrer model

The Monshi-Scherrer model minimizes errors and incorporates all reflections by reformulating the Scherrer equation through logarithmic transformations. According to the published research, Eq. (14**)** provides a detailed mathematical expression of this strategy [26].

View Article Online
DOI: 10.1039/D5MA01083G

$$ln(\beta) = ln\frac{1}{cos\theta} + ln\frac{k\lambda}{D} \quad (14)$$

Plotting $ln(\beta)$ versus ln (1/ $cos\theta$) as per Eq. (14) and aligning with the linear equation ($y = mx + c$), the crystallite size can be assessed from the intercept.

3.2.3. Size-Strain plot model

For assessing the strain and crystallite size in anisotropic crystals, the size-strain plot is a commonly used method. By focusing on low angle diffraction peak with minimal overlap, this method improves the reliability of crystallite size and strain determinations. The associated equation for this model is shown as Eq. (15) in the referenced literature [27].

$$(d_{hkl}\beta_{hkl}cos\theta)^2 = \frac{k\lambda}{D}\left(d_{hkl}^2\beta_{hkl}cos\theta\right) + \frac{\varepsilon^2}{4} \quad (15)$$

By positioning $(d_{hkl}\beta_{hkl}cos\theta)^2$ on the Y-axis and $\left(d_{hkl}^2\beta_{hkl}cos\theta\right)$ on the X-axis. Eq. 15 was then compared to a straight-line equation to estimate the crystallite size, which is derived from the slope.

3.2.4. Linear Straight-Line model

The Scherrer equation only uses the widening of a single diffraction peak to determine the crystallite size. For precise material characterization, comprehensive calculations are therefore essential. The Scherrer equation yields the linear straight model Eq. (16), which is a trustworthy model for evaluating crystallite size [27].

$$\cos(\theta) = \frac{k\lambda}{D} \times \frac{1}{\beta} \quad (16)$$

Crystallite size was obtained from the intercept of the 1/ β versus $\cos(\theta)$.

3.2.5. Sahadat-Scherrer model

Assuming that strain broadening is separable, this model was established by removing the instrumental broadening contributions from the diffraction peak broadening. The Scherrer formula yielded Eq. (17), which shows an algebraic expression related to this model. When the straight line crosses the origin, the model's accuracy rises [29]. The Sahadat-Scherrer model's mathematical representation is as follows:

$$cos\,(\theta) = \frac{k\lambda}{D_{s-s}} \times \frac{1}{FWHM} \quad (17)$$

View Article Online
DOI: 10.1039/D5MA01083G

A linear relationship is obtained by plotting 1/FWHM against $cos\ (\theta)$ results in a straight line that passes through the origin. The resulting straight line passes through the origin, following the form of the equation $(y = mx)$. The size of crystallites can be calculated by associating $k\lambda/D_{s-s}$ with the slope of the equation.

3.2.6. Halder-Wagner method

The Halder-Wagner technique states that XRD reflections are not a blend of the Gaussian and Lorentzian profiles, but rather a combination of both. A Lorentzian function describes the tail part, whereas a Gaussian function fits the peak region. This suggests that a Voigt function can correctly represent the XRD diffraction pattern. The model evaluates strain using the Gaussian component and determines crystallite size using the Lorentzian component. Eq. (18) provides the mathematical foundation for calculating strain and size using this approach [30].

$$\left(\frac{\beta_{hkl}}{d_{hkl}}\right)^2 = \left(\frac{1}{D}\right)\left(\frac{\beta_{hkl}}{d_{hkl}^2}\right)+\left(\frac{\varepsilon}{2}\right)^2 \quad (18)$$

Crystallite size can be evaluated from the slope by plotting $\left(\frac{\beta_{hkl}}{d_{hkl}}\right)^2$ along the Y-axis and $\left(\frac{\beta_{hkl}}{d_{hkl}^2}\right)$ along X-axis using Eq. 18. Halder-Wagner method is based on assumed strain distribution models that are not necessarily applicable to all cases, and its application is comparatively more demanding than simpler approaches, as it requires rigorous analysis and high precision diffraction data [31].

3.3. Zeta Potential and Dynamic Light Scattering

A vial containing 0.1 mg of the generated α-alumina NPs powder and 20.0 ml of deionized water was employed as a dispersion medium. The vial was then placed in an ultrasonic bath for 30.0 minutes in order to assess the zeta potential [POWER SONIC 510, UK; Power: 410 W]. DLS measures the change in scattering intensities at a single point caused by the particle's Brownian motion by directing monochromatic light through the sample cell and measuring the autocorrelation function of the photocurrent at a given angle. In this analysis, a zeta potential analyzer and particle size analyzer [ZSU5700, Malvern Panalytical, UK] were used.

3.4. UV-Visible Spectrophotometry (UV-Vis)

View Article Online
DOI: 10.1039/D5MA01083G

A UV-1800 spectrophotometer [Shimadzu, Japan], was utilized for UV-Vis analysis in the wavelength range of 200-800 nm and a photometric range of -4 to 4 absorbance and transmittance (0 % to 400 %). The sample is exposed to UV and near-visible radiation, and radiation absorbance or transmittance was evaluated according to the principles of the Beer-Lambert law [32]. To formulate the sample solution for UV-Vis spectroscopic analysis, 0.2 mg of the synthesized α-alumina NPs sample was mixed with 4.0 mL of ethanol solution. The Tauc plot approach [33], which is based on the following equation, was used to examine the absorption data:

$$(\alpha h\nu)^n = A\left(h\nu - E_g\right) \quad (19)$$

In this equation, α stands for the absorption coefficient, hν corresponds to the photon energy, E_g is the band gap energy, A is a proportionality constant, and n varies depending on the nature of the electronic transition.

3.5. Thermogravimetric Analysis and Differential Scanning Calorimetry (TGA and DSC)

Simultaneous Thermal Analyzer (STA) 449 F5 Jupiter (Brand: NETZSCH, Germany) was utilized to carry out TGA-DSC analysis. DSC was carried out under a nitrogen atmosphere (for inert condition) at a heating rate of 5 °C/Min, with a resolution of less than 1 µW, depending on the sensor used. DSC records the changes in enthalpy associated with physical or chemical transformations of α-alumina NPs as a function of time or temperature. TGA was conducted on the same instrument under identical conditions, with a mass resolution of 0.025 µg. TGA monitors the mass loss of α-alumina NPs as the temperature increases, providing insight into various thermal decomposition and transformation processes.

3.6. Transmission Electron Microscopy (TEM)

The internal morphology and elemental composition of the synthesized α-alumina NPs were examined using a multipurpose TEM integrated with EDS [JEM2100 Plus, JEOL, Japan]. The instrument operated at an accelerating voltage of 200 kV to ensure adequate electron beam penetration through the samples. The instrument runs on an input voltage of 210-240 VAC at 50 or 60 Hz, with the maximum load capacity of 20 A, an input breaker rated at 25 A, and a short-circuit current rating (SCCR) of 10 kA. Elemental analysis was conducted under same accelerating voltage, and a probe current of 7.475 nA. using EDS at an accelerating voltage of 200.0 kV, with a real time of 53.06 s, live time of 50.00 s, energy range of 0-40 keV, and probe current of 7.47500

View Article Online
DOI: 10.1039/D5MA01083G

nA, Data were collected using a silicon drift detector (SDD) under PHA (pulse height analysis) mode T3, with a 5 % dead time and a counting rate of 4724 counts/sec.

4. Results and Discussions

4.1. Crystallographic Analysis

X-ray diffraction (XRD) is an effective method for evaluating the crystalline structure of powdered materials. It reveals key details such as crystallinity, phase identity, and purity of the sample [34]. Fig. 1 illustrates the XRD pattern obtained for the synthesized α-alumina NPs. The fabricated NPs were verified to have a hexagonal crystal system within the R-3c (No. 167) space group, as confirmed by comparison with the ICDD standard [card number # 01-076-8186]. The investigation aimed to examine the structural properties of the materials utilizing various bases for pH regulation. For samples A and C, eight noticeable diffraction peaks were found. In contrast, additional peaks appeared in sample B due to the presence of KOH-related phases. In Fig. 1 the main diffraction angles for sample A observed at 24.810°, 34.389°, 37.011°, 42.594°, 51.7948°, 56.7189°, 65.748°, and 67.418° align with (0 1 2), (1 0 4), (1 1 0), (1 1 3), (0 2 4), (1 1 6), (2 1 4), and (3 0 0) miller indices. The heights observed for sample A of 7406 cps, 15042 cps, 7327 cps, 17309 cps, 7286 cps, 14860 cps, and 5119 cps. The prominent diffraction peaks noticed for sample B were 25.544°, 34.834°, 36.998°, 43.516°, 51.751°, 56.711°, 65.721°, and 67.412°, while those for sample C were 24.764°, 34.322°, 36.957°, 42.502°, 51.729°, 56.644°, 65.684°, and 67.400°, corresponding to the same Miller indices in both cases. Bishwas et al. reported comparable diffraction peaks associated with the same miller indices [35]. Corresponding peak heights were observed for sample B as 485 cps, 437 cps, 4079 cps, 341 cps, 4199cps, 7501 cps, 2600 cps, and 3834 cps, and for sample C as 6447 cps, 13723 cps, 6383 cps, 14432 cps, 5951 cps, 11742 cps, 3997 cps, and 6848 cps.

View Article Online
DOI: 10.1039/D5MA01083G

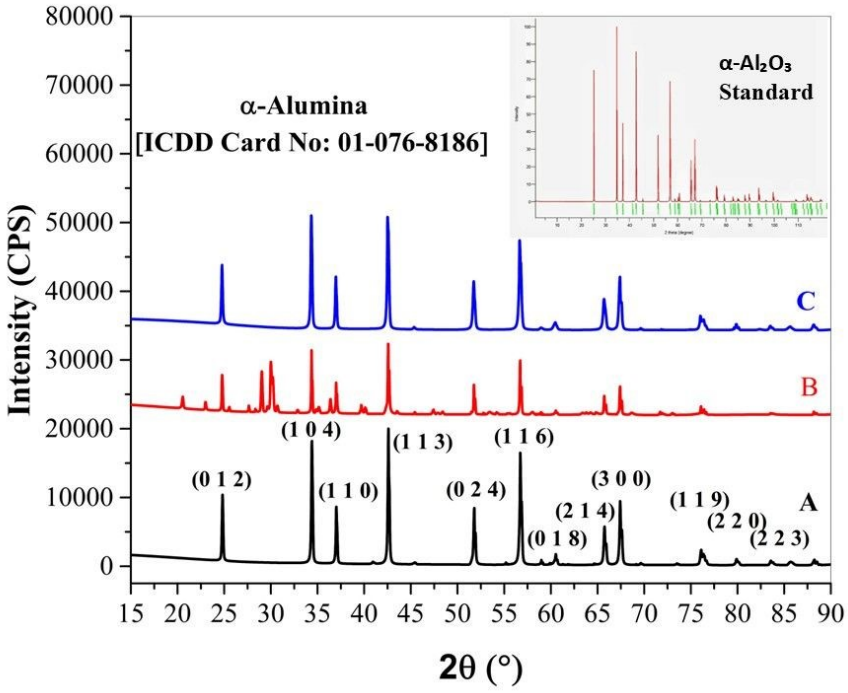

Fig. 1. X-ray diffraction pattern of the prepared α-alumina NPs.

For sample A. the average crystallite size was found to be 68.43 nm for sample A, 94.74 nm for sample B, and 54.67 nm for sample C. Among the three, the smallest crystallite size was exhibited by sample C.

Table 1. Crystallite size calculation of α-alumina NPs.

2Θ (°)	Reflection	FWMH (°)	Intensity (CPS)	Height (CPS)	d-spacing (Å)	Crystal lite size, D, (nm)	Average Crystallite Size (nm)
NaOH Base (Sample: A)							
24.810	(0 1 2)	0.127	1230	7406	3.5858	66.7	
34.389	(1 0 4)	0.125	2544	15042	2.6058	69.4	
37.011	(1 1 0)	0.111	1166	7327	2.42692	78.8	
42.594	(1 1 3)	0.123	3078	17309	2.12085	72.5	68.43
51.7948	(0 2 4)	0.125	1149	7286	1.76366	70.0	
56.7189	(1 1 6)	0.125	3003	14860	1.62167	75.1	

View Article Online
DOI: 10.1039/D5MA01083G

65.748	(2 1 4)	0.158	1197	5119	1.41913	62.5	
67.418	(3 0 0)	0.138	1844	8732	1.38799	72.5	
kOH Base (Sample: B)							
25.544	(0 1 2)	0.099	56	485	3.4844	85.5	
34.360	(1 0 4)	0.072	842	8617	2.6078	121.1	
36.998	(1 1 0)	0.073	548	4079	2.4278	119.7	
42.576	(1 1 3)	0.079	1027	9267	2.1217	113.1	94.74
51.751	(0 2 4)	0.080	465	4199	1.76503	115.9	
56.711	(1 1 6)	0.088	981	7501	1.62189	107.7	
65.721	(2 1 4)	0.092	361	2600	1.41965	106.8	
67.412	(3 0 0)	0.106	468	3834	1.38810	94.2	
NH_4OH Base (Sample: C)							
24.764	(0 1 2)	0.131	1203	6447	3.5923	64.9	
34.322	(1 0 4)	0.139	2647	13723	2.6107	62.4	
36.957	(1 1 0)	0.131	1175	6383	2.4303	66.7	
42.502	(1 1 3)	0.153	3107	14432	2.12524	58.2	54.67
51.729	(0 2 4)	0.183	1525	5951	1.76574	50.5	
56.644	(1 1 6)	0.173	2943	11742	1.62364	54.6	
65.684	(2 1 4)	0.218	1152	3997	1.42037	45.3	
67.400	(3 0 0)	0.184	1771	6848	1.38831	54.2	

The main diffractions for the nanocrystal at 34.799° (1 0 4), 42.903° (1 1 3), and 56.890° (1 1 6) in the ICDD data revealed a slight leftward shift to 34.389°, 42.594°, and 56.719° for sample A, and 34.322°, 42.502°, and 56.644° for sample C. Conversely, rightward shift observed for sample B this contraction is typically associated with a reduced unit cell volume, which shortens the distance between atomic planes. As a result, the Bragg angle increases, causing a rightward shift in the diffraction peaks due to constructive interference at higher 2θ values. whereas diffraction shifted to 34.834°, 42.502° and 56.644°. A shift toward lower 2θ angles indicates an increase in interplanar spacing, implying lattice expansion within the crystal structure. The expansion is commonly linked to an increase in the unit cell volume, which enlarges the distance between atomic planes. This greater spacing reduces the Bragg angle, resulting in a leftward shift of the

View Article Online
DOI: 10.1039/D5MA01083G

diffraction peaks due to enhanced constructive interference. In contrast, rightward shift indicates a decrease in interplanar spacing [36][37].

Table 2 and **Table 3** present the peak indexing calculation using theta (θ) and inter-planar distance. Three primary diffraction peaks were identified at 2θ = 34.389°, 42.594° and 56.719° for sample A. For sample B, the peaks occurred at 2θ values of 34.834°, 42.502° and 56.644°, while sample C showed peaks in the plane of (1 0 4), (1 1 3) and (1 1 6) which are completely similar to the standard data [ICDD Card No: 01-076-8186] crystal plane. The peak profiling information for the synthesized NPs, determined using the diffraction angle (θ), is summarized in **Table 2**. The calculated profile values suggest a uniform atomic distribution along specific crystal planes (Miller indices), indicating a preferred crystallographic orientation. Furthermore, the d-spacing-based peak analysis presented in **Table 3** supports this observation, confirming preferential growth within the α-alumina NPs crystal structure [38][39].

Table 2. Profiling of diffraction peaks based on the diffraction angle (θ).

2Θ	Θ	1000× Sin^2 Θ	Reflection	Remarks
		NaOH Base (A)		
34.389	17.195	87.3939	(1 0 4)	$1^2+0^2+4^2=17$
42.594	21.297	131.9160	(1 1 3)	$1^2+1^2+3^2=11$
56.719	28.3595	225.6271	(1 1 6)	$1^2+1^2+6^2=38$
		KOH Base (B)		
34.834	17.417	89.5948	(1 0 4)	$1^2+0^2+4^2=17$
42.576	21.288	131.8097	(1 1 3)	$1^2+1^2+3^2=11$
56.711	28.355	225.5615	(1 1 6)	$1^2+1^2+6^2=38$
		NH_4OH Base (C)		
34.322	17.161	87.0590	(1 0 4)	$1^2+0^2+4^2=17$
42.502	21.251	131.373	(1 1 3)	$1^2+1^2+3^2=11$
56.644	28.322	225.08	(1 1 6)	$1^2+1^2+6^2=38$

Table 3. Diffraction peak profiling by interplanar distance or d-spacing (d).

View Article Online
DOI: 10.1039/D5MA01083G

2Θ	Θ	d-spacing (Å)	1000/d²	Reflection	Remarks
		NaOH Base (A)			
34.389	17.195	2.6058	147.2712	(1 0 4)	$1^2+0^2+4^2=17$
42.594	21.297	2.1209	222.3207	(1 1 3)	$1^2+1^2+3^2=11$
56.719	28.3595	1.6217	380.2551	(1 1 6)	$1^2+1^2+6^2=38$
		KOH Base (B)			
34.834	17.417	2.5735	150.9912	(1 0 4)	$1^2+0^2+4^2=17$
42.576	21.288	2.1217	222.1427	(1 1 3)	$1^2+1^2+3^2=11$
56.711	28.355	1.6219	380.1519	(1 1 6)	$1^2+1^2+6^2=38$
		NH_4OH Base (C)			
34.322	12.650	2.6107	146.7189	(1 0 4)	$1^2+0^2+4^2=17$
42.502	19.088	2.1252	221.4033	(1 1 3)	$1^2+1^2+3^2=11$
56.644	23.935	1.6236	379.3329	(1 1 6)	$1^2+1^2+6^2=38$

Table 4. Estimated crystallographic parameters of the synthesized α-alumina NPs.

Parameters	Sample A	Sample B	Sample C
Average crystallite size (nm)	68.43	94.74	54.67
Microstrain	0.000250	0.000179	0.00327
Lattice parameters	a=b=4.8267 Å, c= 13.102Å	a=b=4.8002 Å, c= 13.117 Å	a=b=4.8324 Å, c= 13.178 Å
Angular parameters	α = β = 90°, γ=120°	α = β = 90°, γ=120°	α = β = 90°, γ=120°
Crystallinity (%)	35.69	36.02	35.73
Lattice volume (Å³)	264.344	261.738	266.516
Crystal strain (%)	0.150	0.153	0.174
Dislocation density (nm^{-2})	0.000217	0.000120	0.000351
Specific surface area ($m^2\ g^{-1}$)	22.66	16.36	28.36
Crystallinity Index	2.727	2.104	2.764
Preference Growth	0.132	0.544	0.114

4.1.2. Quantitative analysis by Rietveld refinement in WPPF method

As shown in **Fig. 2**, the Whole Powder Pattern Fitting (WPPF) technique applies detailed crystal structure and lattice constant information to perform profile fitting across an extensive angular span. This approach enables the concurrent refinement of both diffraction intensity and angle

View Article Online
DOI: 10.1039/D5MA01083G

during the pattern fitting process [40]. The experimental XRD data were compared against the reference pattern for α-Alumina NPs (ICDD Card No: 01-076-8186). Rietveld refinement using the WPPF method confirmed that samples A, B, and C consisted entirely (100.0%) of the α-Alumina phase, exhibiting a hexagonal crystal structure.

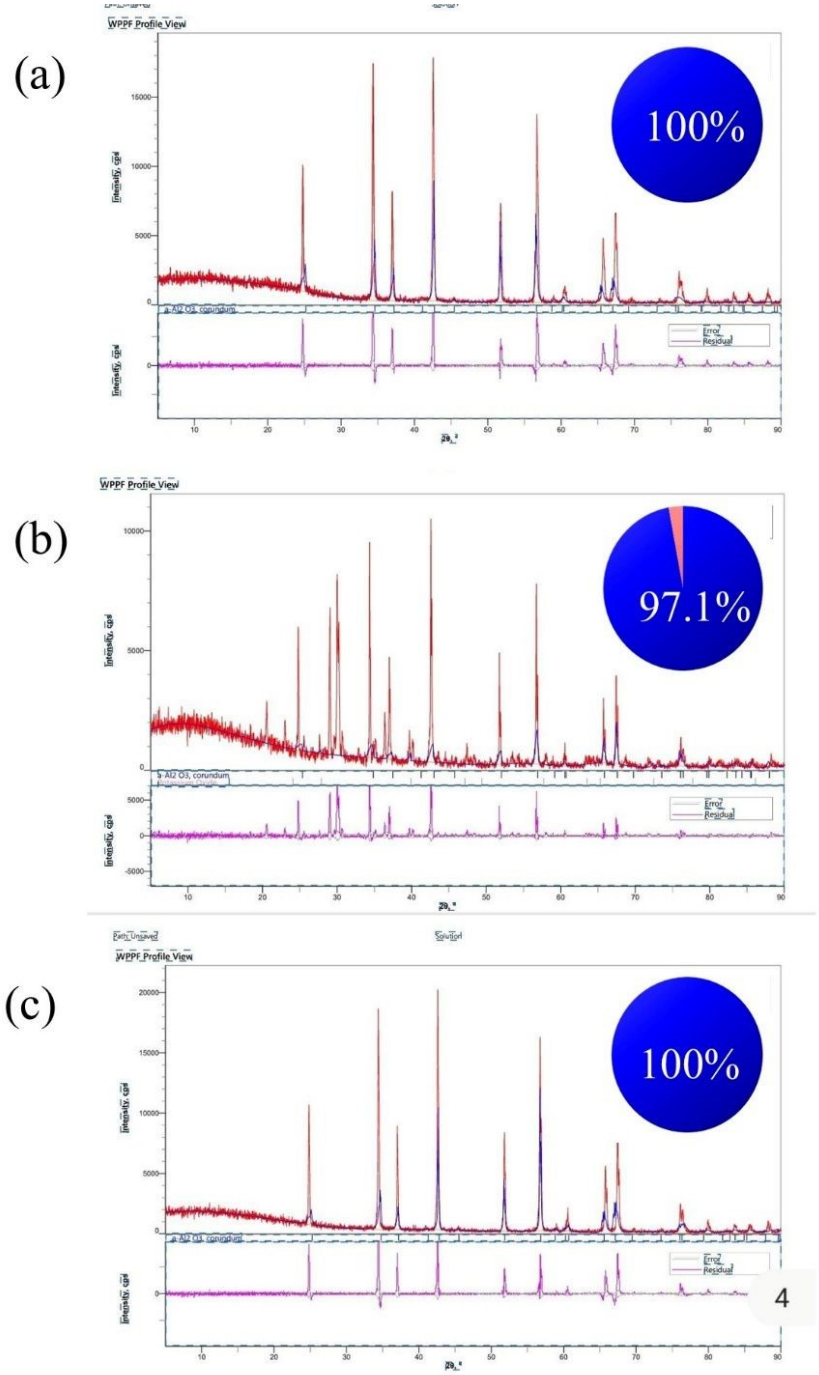

Fig. 2. Quantitative analysis of α-alumina NPs by WPPF method.

View Article Online
DOI: 10.1039/D5MA01083G

Fig. 2 illustrates the synthesis of 100 % α-Alumina NPs for sample A and C and 97.1% α-Alumina NPs with 2.9% potassium oxide for sample B under varying fitting conditions, where (Rwp, 46.34% %; Rp, 31.43 %; S 1.8121; χ^2 3.2836 for sample A, Rwp, 41.26% %; Rp, 29.29 %; S 1.5154; χ^2 2.2963, for sample B and Rwp, 44.46 % %; Rp, 31.32 %; S 1.7806; χ^2 3.1705 for sample C). Crystal lattice parameters were obtained through structural refinement using the Rietveld approach. The refined lattice parameters for the nanoparticles were determined to be a = b = 4.8267 Å, c = 13.1019 Å (sample A), a = b = 4.8002 Å, c = 13.117 Å (sample B), and a = b = 4.8324 Å, c = 13.187 Å (sample C), all with α=β= 90.0°, γ=120. 0°. In contrast, the corresponding standard values were a = b = 4.807 Å, c = 13.116 Å; α=β= 90.0° γ=120.

Table 5. Comparison study and quantitively analysis of synthesized α-alumina NPs.

Comparison study of Experimental (Exp.) and Standard (Std.) Diffraction Data for sample A							
2Θ (Exp.)	**2Θ (Std.)**	**d (Å) (Exp.)**	**d (Å) (Std.)**	**Intensity, I (cps) (Exp.)**	**Intensity, I (cps) (Std.)**	**Crystallinity (%) (Exp.)**	**Crystallinity (%) (Std.)**
34.389	34.799	2.6058	2.57591	82.66	100.0	35.69	33.92
42.594	42.904	2.1209	2.10621	100.00	98.6		
56.719	56.890	1.6217	1.61717	97.56	96.2		
Quantitively analysis by WPPF method							
Pattern fitting condition		**Lattice volume, (Å³)**		**Strain (%)**	**Phase (%)**	**Lattice parameter**	
Rwp, 46.34% %; Rp, 31.43 %; S 1.8121; χ^2 3.2836		264.344		0.15	100 [Corundum]	a=b=4.8267 Å, c= 13.1019Å; α=β= 90.0°,γ=120. 0°	
Lattice parameter [Corundum: 01-076-8186] (std.)		a=b=4.807 Å, c= 13.116 Å; α=β=90.0°,γ=120.0°; Volume: 262.47 Å³; MolVol:34.01; Calculated density: 3.87 g/cm³; Structural density: 3.87 g/cm³; Space Group: R-3c (167).					
Comparison study of Experimental (Exp.) and Standard (Std.) Diffraction Data for sample B							
2Θ (Exp.)	**2Θ (Std.)**	**d (Å) (Exp.)**	**d (Å) (Std.)**	**Intensity, I (cps) (Exp.)**	**Intensity, I (cps) (Std.)**	**Crystallinity (%) (Exp.)**	**Crystallinity (%) (Std.)**

View Article Online
DOI: 10.1039/D5MA01083G

34.834	34.799	2.5735	2.5759	82.03	100.0		
42.576	42.904	2.1217	2.1062	100.00	98.6	36.02	33.92
56.711	56.890	1.6219	1.6172	95.58	96.2		

Pattern fitting condition	**Lattice volume, (Å³)**	**Strain (%)**	**Phase (%)**	**Lattice parameter**
Rwp, 41.26% %; Rp, 29.29 %; S 1.5154; χ^2 2.2963	261.738	0.1526%	97.1 [Corundum]	a=b=4.8002 Å, c= 13.117 Å; α=β= 90.0°, γ= 120.0°

Comparison study of Experimental (Exp.) and Standard (Std.) Diffraction Data for sample C

2Θ (Exp.)	**2Θ (Std.)**	**d (Å) (Exp.)**	**d (Å) (Std.)**	**Intensity, I (cps) (Exp.)**	**Intensity, I (cps) (Std.)**	**Crystallinity (%) (Exp.)**	**Crystallinity (%) (Std.)**
34.322	34.799	2.6107	2.57591	85.19	100.0		
42.502	42.904	2.1252	2.10621	100.00	98.6	35.73	33.92
56.644	56.890	1.6236	1.61717	94.72	92.2		

Quantitively analysis by WPPF method

Pattern fitting condition	**Lattice volume, (Å³)**	**Strain (%)**	**Phase (%)**	**Lattice parameter**
Rwp, 44.46 % %; Rp, 31.32 %; S 1.7806; χ^2 3.1705	266.516	0.174	100 [Corundum]	a=b=4.8324 Å, c= 13.178 Å; α=β=90.0°, γ= 120.0°

4.1.3. Crystallite size estimation employing multiple models

Several analytical models, such as Williamson-Hall plot, Monshi-Scherrer method, Size-strain plot model, Linear-straight-line model, Sahadat-Scherrer model and Halder-Wagner method **(refer to Eqs. 13–18)**, were applied to determine the crystallite size of the synthesized α-alumina NPs sample A, B and C. Their crystallite sizes were summarized in **Table 6**.

The Williamson-Hall plot extends the Scherrer equation by incorporating the impact of microstrain in the crystal lattice, which also contributes to peak broadening. It is assumed that the overall broadening of X-ray diffraction peaks results from a combination of size-induced broadening and

View Article Online
DOI: 10.1039/D5MA01083G

strain effects, which is caused by the limited crystallite size, and strain broadening, which is caused by lattice distortions, or microstrain, in the material forms the basis of the Williamson-Hall plot.

Through the analysis of several diffraction peaks, the Monshi-Scherrer model enhances crystallite size determination by enabling precise average size and taking crystal anisotropy into concern. The Scherrer equation was modified to minimize mistakes and incorporate all reflections for determining crystallite size by rearranging it and applying the logarithm to both sides. For nanoscale materials with high strain, this minimizes the inaccuracies common in conventional Scherrer calculations. Averaging several diffraction peaks along with partial correction for anisotropic broadening leads to an increased calculated crystallite size that was achieved using this model as opposed to the conventional Scherrer eq. The model's multi-peak structure tends to lessen the underestimate seen in single-peak approaches, offering a more precise estimate for nanomaterials with moderate strain even though it does not specifically account for microstrain.

The Size Strain Plot model analyzes strain effects and crystallite size in a single computation by using a linear plot. This yields a more accurate approximation than approaches that presume that strain or size alone is the cause of broadening. The SSP model is appropriate for materials having anisotropic (direction-dependent) characteristics since it takes into consideration several crystal planes. By using many peaks, the errors that come from depending just on one diffraction peak are decreased. The SSP model reduces these assumptions, producing a more precise assessment of crystallite size and strain, in contrast to the Scherrer model, which assumes that peak broadening is mostly caused by crystallite size. This is particularly helpful for materials at the nanoscale, where peak broadening is greatly influenced by both factors.

The linear straight-line model, a variant of the Scherrer model, is widely used to estimate crystallite size. In contrast to other models, this approach produced a noticeably bigger crystallite size, suggesting that this material system is not very reliable. The primary limitation arises from the model’s assumption of negligible strain and instrumental broadening effects, which causes systems where peak broadening is not exclusively attributable to crystallite dimensions to overestimate size. The model's applicability for α-alumina is further diminished by the significant deviation in linear fitting introduced by the substantial variety in peak widths across various reflections.

Sahadat-Scherrer model calculates crystal size more accurately in order to get around the drawbacks of the linear straight-line model. There are multiple crystallite size restrictions

View Article Online
DOI: 10.1039/D5MA01083G

(crystallite size with a larger value) depicted in the models discussed above. Thus, it is essential to overcome these restrictions. That is why the Sahadat-Scherrer model is illustrated. One benefit of this model is that it provides a more accurate crystal size since it accounts for the straight line that passes through the origin. Estimated crystallite sizes are in good agreement with results from traditional Scherrer equation, demonstrating that this approach effectively minimizes overestimation without compromising analytical ease.

According to the Halder-Wagner technique, the XRD reflection is a combination of both a Lorentzian and a Gaussian function. This approach states that a Lorentzian function governs the reflection's tail. It is suggested that a Voigt function can explain the XRD diffraction because the peak simultaneously conforms to a Gaussian function. In this model, the strain is estimated using the Gaussian equation, and the crystallite size is determined using the Lorentzian function. The Halder-Wagner method's mathematical formulation for calculating size and strain.

View Article Online
DOI: 10.1039/D5MA01083G

393 **Table 6.** Calculated crystallite sizes of the synthesized α-alumina using various models

Methods Name	Crystallite size (nm) for sample A	Correlation Coefficient (R^2)	Crystallite size (nm) for sample B	Correlation Coefficient (R^2)	Crystallite size (nm) for sample C	Correlation Coefficient (R^2)
Williamson-Hall plot	69.69	-0.1558	73.38	0.06148	85.08	-0.1558
Monshi-Scherrer method	70.04	0.437	84.49	-0.166	64.92	0.8151
Linear-straight-line model	249.06	-0.1663	307.17	0.01759	167.27	0.1951
Sahadat-Scherrer model	75.37	0.9796	105.87	0.9523	61.09	0.9780
Size-strain plot	63.04	0.9959	74.56	0.9732	67.98	0.9757
Halder-Wagner method	96.47	0.994	81.54	0.968	89.99	0.981

394

395

396 Among the models applied, the Size-Strain plot and Halder-Wagner models demonstrated the
397 best correlation, as evidenced by their highest R^2 values during analysis.

398

399 ***4.1.4. Structural Mechanism***

View Article Online
DOI: 10.1039/D5MA01083G

The structures illustrated in **Fig. 3** were created with the aid of VESTA software, based on structural parameters for Al_2O_3 NPs, Al atom is located x=0.000, y=0.333 and z=0.000 and O atom x=0.166, y=0.166 and z=0.220. α-Alumina (Al_2O_3) exhibits a hexagonal crystal structure and belongs to the rhombohedral space group R-3C (space group number 167). The structural visualization using VESTA software provided a clear representation of the α-alumina NPs crystal framework. Ball-and-stick and plane model visualizations reinforced the identification of dominant atomic arrangements and confirmed uniformity across samples in terms of crystallographic symmetry and atomic coordination. **Fig. 3** demonstrates the crystal structure dominant plane of α-alumina NPs where **3(a), 3(b)** and **3(c)** depict the ball-and-stick representations for samples A, B, and C, respectively, while **3(d)** to **3(f)** illustrate the corresponding predominant planes.

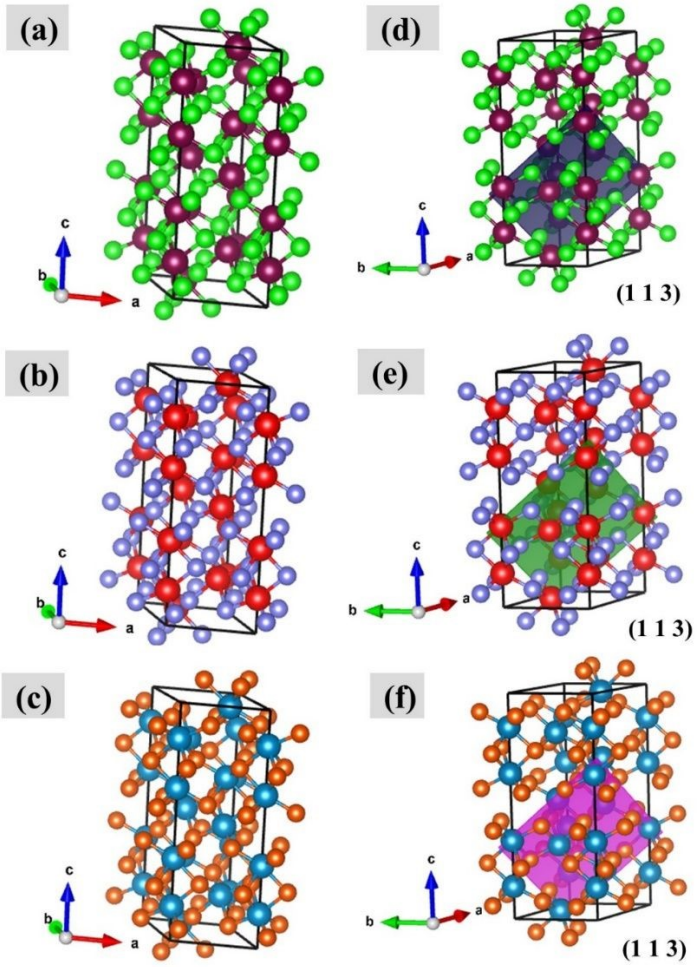

Fig. 3. Crystal structure of the synthesized α-alumina NPs (a) sample A, (b) sample B, and (c) sample C, and (d), (e), (f) their corresponding crystal plane (1 1 3).

View Article Online
DOI: 10.1039/D5MA01083G

A strong diffraction peak observed along the (113) plane indicates a preferred orientation and significant atomic alignment in this direction [41]. The angular parameters remain consistent across all samples, with α = β = 90.00° and γ = 120.00°. The lattice parameters for the samples are as follows: sample A exhibits a=b=4.8267 Å and c= 13.1019Å; sample B shows a=b=4.8002 Å and c= 13.117 Å; and sample C has a=b=4.8324 Å, c= 13.178 Å. For all three samples, the highest intensity diffraction peak is observed along the (113) plane, indicating a preferred crystallographic orientation and suggesting a higher degree of atomic alignment in this direction.

4.2. Band gap Analysis

The optical band gap of α-alumina NPs was evaluated using the Tauc plot method **(Eq. 19)**, as shown in **Fig. 4**, where $(\alpha h\vartheta)^n$was plotted against hν. The band gap energy was determined by extrapolating the linear segment of the curve to the photon energy axis. The extrapolation yielded a calculated band gap of the synthesized NPs. The best linear fit was obtained for n=2, confirming an allowed indirect transition [42]. This value aligns with the characteristic band gap range of the α-alumina phase, typically reported between 5.0 to 6.0 eV [43]. The slight differences in band gap values may be attributed to variations in crystallite size, lattice strain, and surface defects introduced during synthesis. Synthesized NPs exhibit a wide band gap of about 5.4-5.5 eV, indicating strong insulating behavior. Its excellent thermal conductivity and chemical inertness further support its integration in electronic, optical, and high-temperature technologies [43]. These combined properties make it highly desirable for advanced functional applications. A material with a higher band gap energy typically has stronger atomic bonds, which increases the material's mechanical strength. Wide band gaps in nanoparticles are usually associated with higher hardness and thermal stability. Among the synthesized samples, sample C exhibited the highest band gap energy (5.58 eV), followed by sample A (5.53 eV) and sample B (5.54 eV).

View Article Online
DOI: 10.1039/D5MA01083G

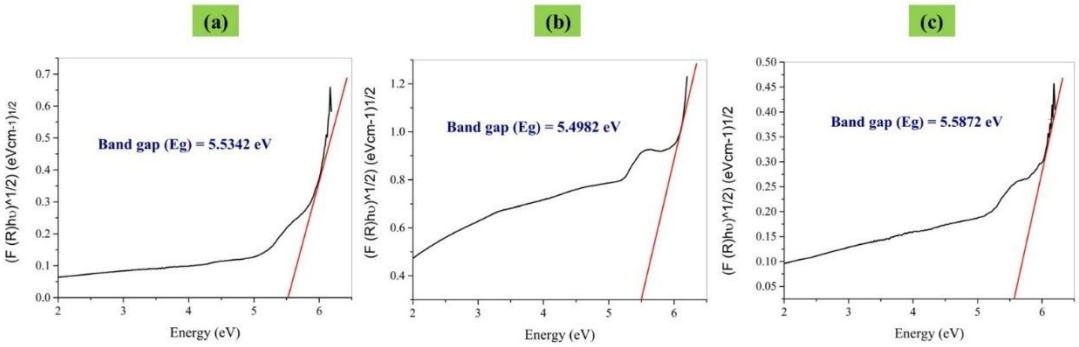

Fig. 4. Tauc's curve for band gap of (a) sample A, (b) sample B and (c) Sample C.

4.4 Hydrodynamic Diameter and Zeta Potential Analysis

Fig. 5. presents the size distribution scatter pattern acquired through DLS analysis. Panels **5(a)**, **5(b)**, and **5(c)** correspond to the DLS size distribution results for samples A, B, and C, respectively. Dynamic light scattering (DLS) was conducted to evaluate the hydrodynamic diameter of the prepared α-alumina NPs [45] [46] [47]. The hydrodynamic diameters were 492.3 nm for sample A, 420.0 nm for sample B, and 418.12 nm for sample C, indicating relatively comparable size distributions among the samples. The nanoparticles synthesized with NH_4OH base (sample C) showed a polydispersity index (PDI) of o.4341, reflecting slight agglomeration, yet the majority of particles were predominantly within the nanoscale domain. Nanoparticles synthesized with using NaOH base (sample A, PDI 0.516) and KOH base (sample B, PDI 0.6124) exhibited higher polydispersity, reflecting increased heterogeneity in particle size. This reflects greater agglomeration and less controlled growth compared to those produced with NH_4OH as the base.

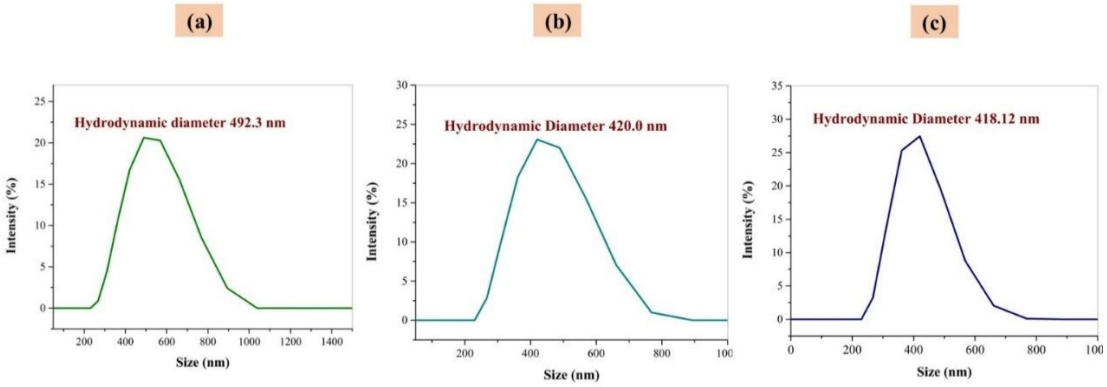

View Article Online
DOI: 10.1039/D5MA01083G

Fig. 5. Particle size distribution curves **(a)** for sample A, **(b)** for sample B, and **(c)** for sample C.

Sample C demonstrated the smallest hydrodynamic diameter among all samples, indicating better dispersion and lower agglomeration compared to samples A and B.

Fig. 6 represents the zeta potential measurements obtained by electrophoretic light scattering (ELS), where panels **6(a)**, **6(b)**, and **6(c)** corresponds to samples A, B, and C, respectively. In general, any particles that have a zeta potential higher than ±30 mV are typically remain electrostatically stable [48].

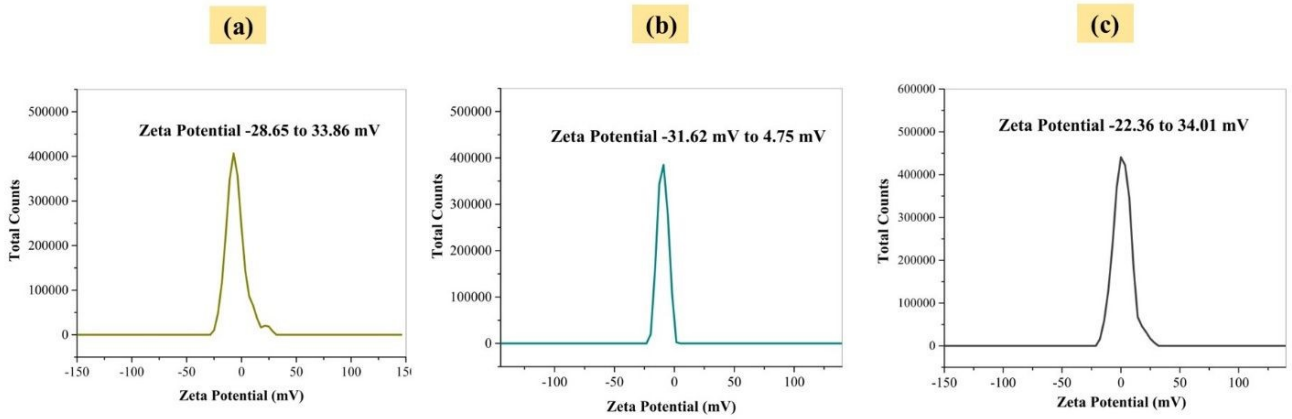

Fig. 6. Zeta potential distribution curves **(a)** for sample A, **(b)** for sample B, and **(c)** for sample C.

Sample A demonstrated a zeta potential range from –28.65 mV to 33.86 mV, whereas sample B exhibited a narrower range of –31.62 mV to +4.75 mV, and sample C showed a range from –22.36 mV to +34.01 mV. Zeta potential measurements revealed that samples prepared with NaOH and NH_4OH base exhibited broader potential ranges, indicating superior colloidal stability.

DLS analysis indicated that sample C possessed the smallest hydrodynamic diameter, reflecting better particle dispersion and reduced agglomeration, whereas sample A exhibited the largest size. ELS results showed that samples A and C had wider zeta potential ranges, suggesting improved colloidal stability relative to sample B. These findings highlight the significant role of the base in

View Article Online
DOI: 10.1039/D5MA01083G

controlling both hydrodynamic diameter and surface charge, with NH_4OH promoting finely dispersed particles and both NaOH and NH_4OH base enhancing electrostatic stabilization.

These samples maintained particle dispersibility due to higher surface charges, which is advantageous for applications involving suspensions or coatings. In contrast, the KOH-based sample showed a narrower potential range, implying reduced electrostatic repulsion and lower stability.

4.5. Thermogravimetric and Differential Scanning Calorimetric Analysis

TGA-DSC curves of the synthesized NPs (**Fig. 7-9**) reveal multiple stage mass loss behavior associated with the stepwise dihydroxylation of $Al(OH)_3$ to Al_2O_3. In sample A, as it can be seen from TGA curve, mass loss began at approximately 89.19 °C and was completed around 1140.24 °C, giving a total reduction of 38.96%. Distinct stages were identified: 17.57 % (86.84 ^{0}C-254.62^{0}C), 10.14 % (255.12 ^{0}C-445.63 ^{0}C), 4.64 % (446.21 ^{0}C-725.35 ^{0}C), and 5.67% (726.57 ^{0}C-1123.80 ^{0}C). The cumulative mass loss corresponds to the release of volatile decomposition products, confirming that thermal decomposition proceeds through the elimination of water components and ultimately yields aluminum oxide as the sole product. The substantial residual mass of 61.04 % up to 1200 ^{0}C temperature reflects better thermodynamic resistance during subsequent high temperature processing. In case of sample B, decomposition initiated at 86.39 °C and finished near 1091.37 °C, with a cumulative loss of 65.27%. Sequential reductions were 25.45 % (86.39 ^{0}C-209.6 ^{0}C), 15.17 % (210.29 ^{0}C-286.45 ^{0}C), 13.90 % (287.82 ^{0}C-619.10 ^{0}C), 6.85% (620.13 ^{0}C-788.94 ^{0}C), and 5.47% (789.59 ^{0}C-1091.37 ^{0}C). The higher overall mass loss compared with sample A is attributed to water evolution and volatile impurities, including potassium oxide species. The residual mass at 1200 ^{0}C was 34.73 %. For sample C, thermal decomposition started at 81.70 °C and concluded by 1033.86 °C, resulting in a total weight loss of 55.72%. Individual stages comprised 25.71 % (81.70 ^{0}C-)260.92^{0}C, 13.64 % (261.61 ^{0}C-460.98 ^{0}C), 13.84 % (461.04 ^{0}C-912.41 ^{0}C), and 2.54% (913.53 ^{0}C-1033.28 ^{0}C). A final mass of 44.28 % remained at 1200 ^{0}C, indicating moderate thermal resilience.

View Article Online
DOI: 10.1039/D5MA01083G

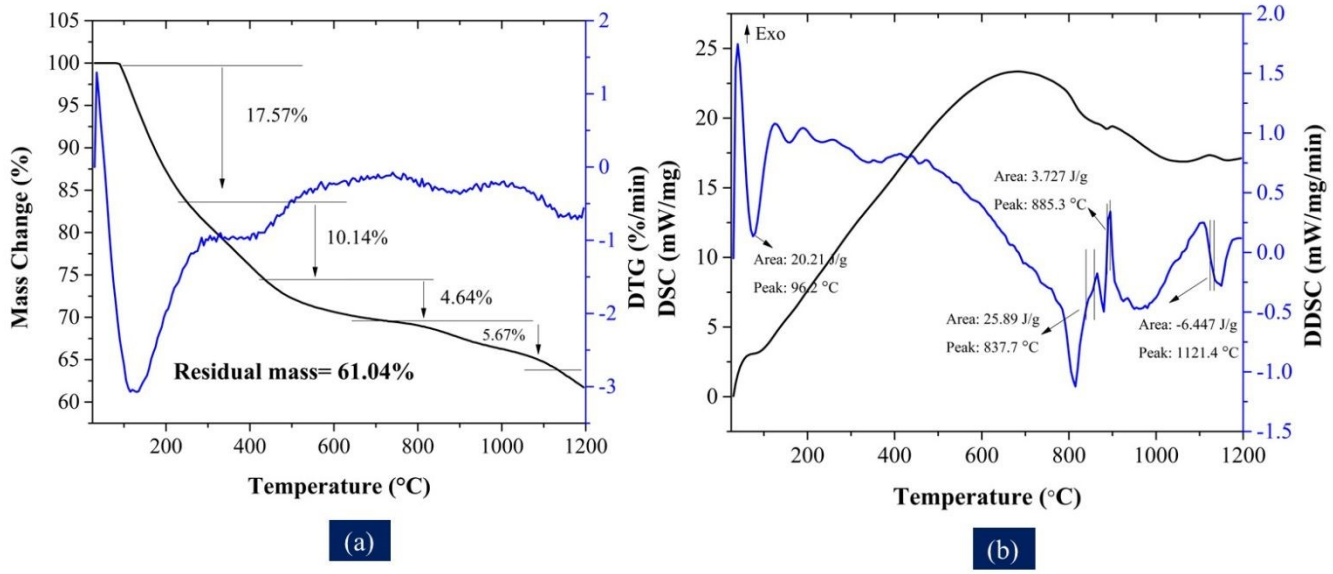

503

504 **Fig. 7.** (a) Thermogravimetric and (b) differential scanning calorimetric analysis of sample A.

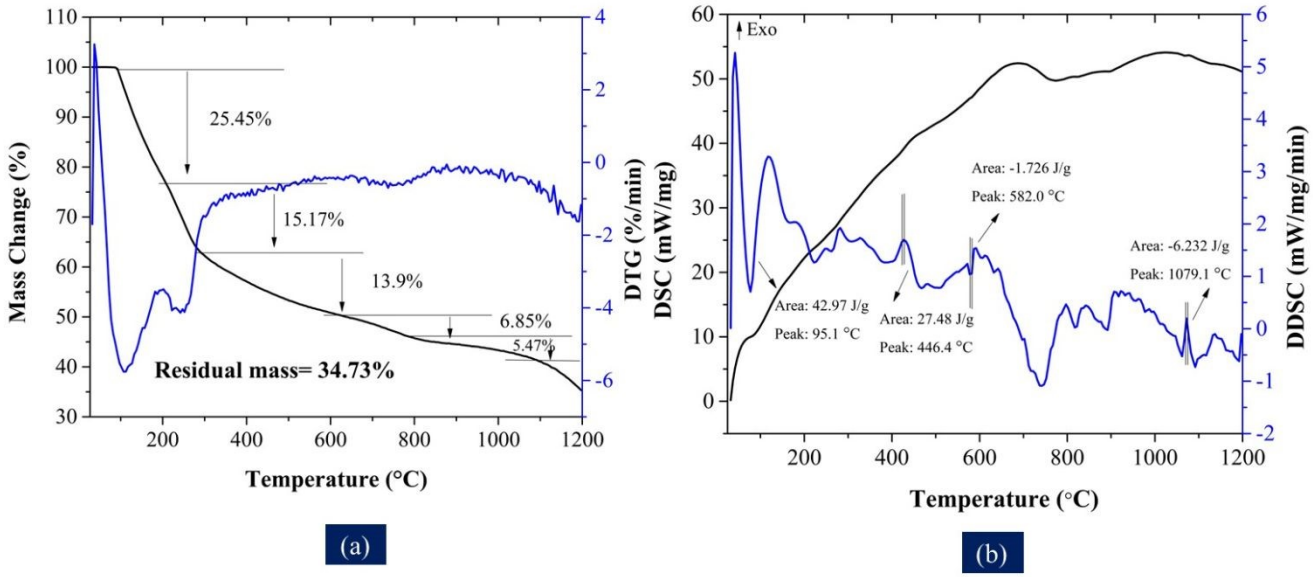

505

506 **Fig. 8.** (a) Thermogravimetric and (b) differential scanning calorimetric analysis of sample B.

507

View Article Online
DOI: 10.1039/D5MA01083G

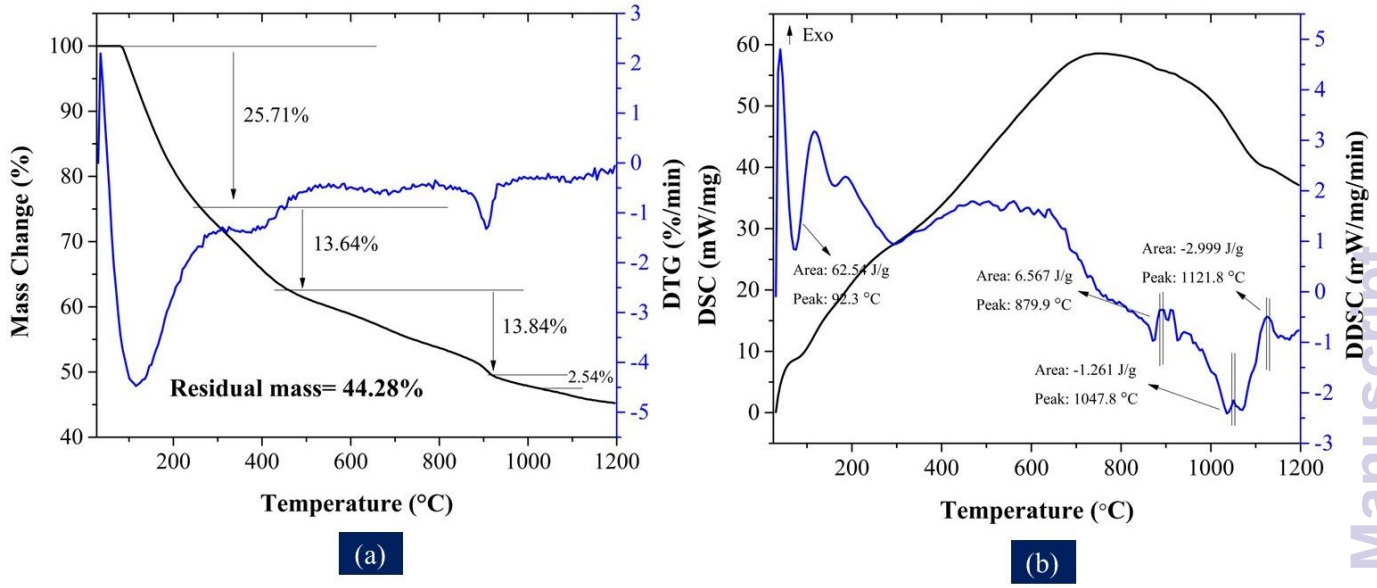

Fig. 9. (a) Thermogravimetric and (b) differential scanning calorimetric analysis of sample C.

The thermal phase transitions of $Al(OH)_3$ were investigated by differential scanning calorimetry (DSC) over the temperature range of 30°C to 1200°C. **Figure 7-9** presents the DSC curves of samples A, B, and C. For sample A, an endothermic feature extending from about 51.87°C to 112.41 °C, is associated with the release of physically bound water. [49]. The DSC curve displays an endothermic peak at 885°C is attributed to the γ-Al_2O_3 to δ-Al_2O_3 phase transition. A subsequent exothermic event near 1121.4°C signifies the formation of the α-Al_2O_3 phase [50]. For sample B, the DSC curve shows a broad endothermic feature from about 54.22°C to 103.28 °C, attributed to the release of physically absorbed water. An endothermic peak at 446.4°C followed by an exothermic peak at 582.0°C is associated with the presence of impurities. An exothermic peak at approximately 1075.1°C indicates the onset of α-Al_2O_3 crystallization. In case of sample C, the DSC profile shows a broad endothermic feature between 51.87°C and 100.93 °C, corresponding to the removal of physically bound water. An endothermic peak at 873.9°C is attributed to the γ-Al_2O_3 to δ-Al_2O_3 phase transition. Formation of α-Al_2O_3 is indicated by the exothermic peaks observed at 1047.5°C and 1121.4°C. In comparision of TGA-DSC among the three samples, saple A showed the lowest mass loss (38.96%) and highest residual mass (61.04%), indicating superior thermal stability, while sample B had the highest mass loss (65.27%) due to

View Article Online
DOI: 10.1039/D5MA01083G

volatile impurities. Sample C exhibited intermediate behavior (55.72% mass loss). DSC analysis revealed slight differences in the γ-Al_2O_3 to δ-Al_2O_3 transition temperatures, whereas α-Al_2O_3 formation occurred between 1047-1121°C.

4.6. Transmission Electron Microscopy Analysis

4.5.1 Internal morphology analysis

TEM analysis was carried out to examine the internal morphology of the synthesized α-alumina nanoparticles [51]. As shown in Fig. 10a–c, the particles predominantly displayed faceted hexagonal domains, consistent with the crystallographic structure of α-alumina. Some regions exhibited partial fusion, which we attribute to agglomeration during calcination. To obtain reliable particle size distributions, measurements were performed on well-dispersed regions of the micrographs, and more than 150 particles were analyzed using ImageJ. The histograms (Fig. 10d–f) follow a Gaussian distribution, yielding average particle sizes of 71.34 nm for sample A, 95.78 nm for sample B, and 57.48 nm for sample C, confirming their nanoscale dimensions. Notably, particle sizes observed by TEM were larger than the crystallite sizes estimated from XRD, indicating that individual TEM-observed particles consist of multiple crystallites.

View Article Online
DOI: 10.1039/D5MA01083G

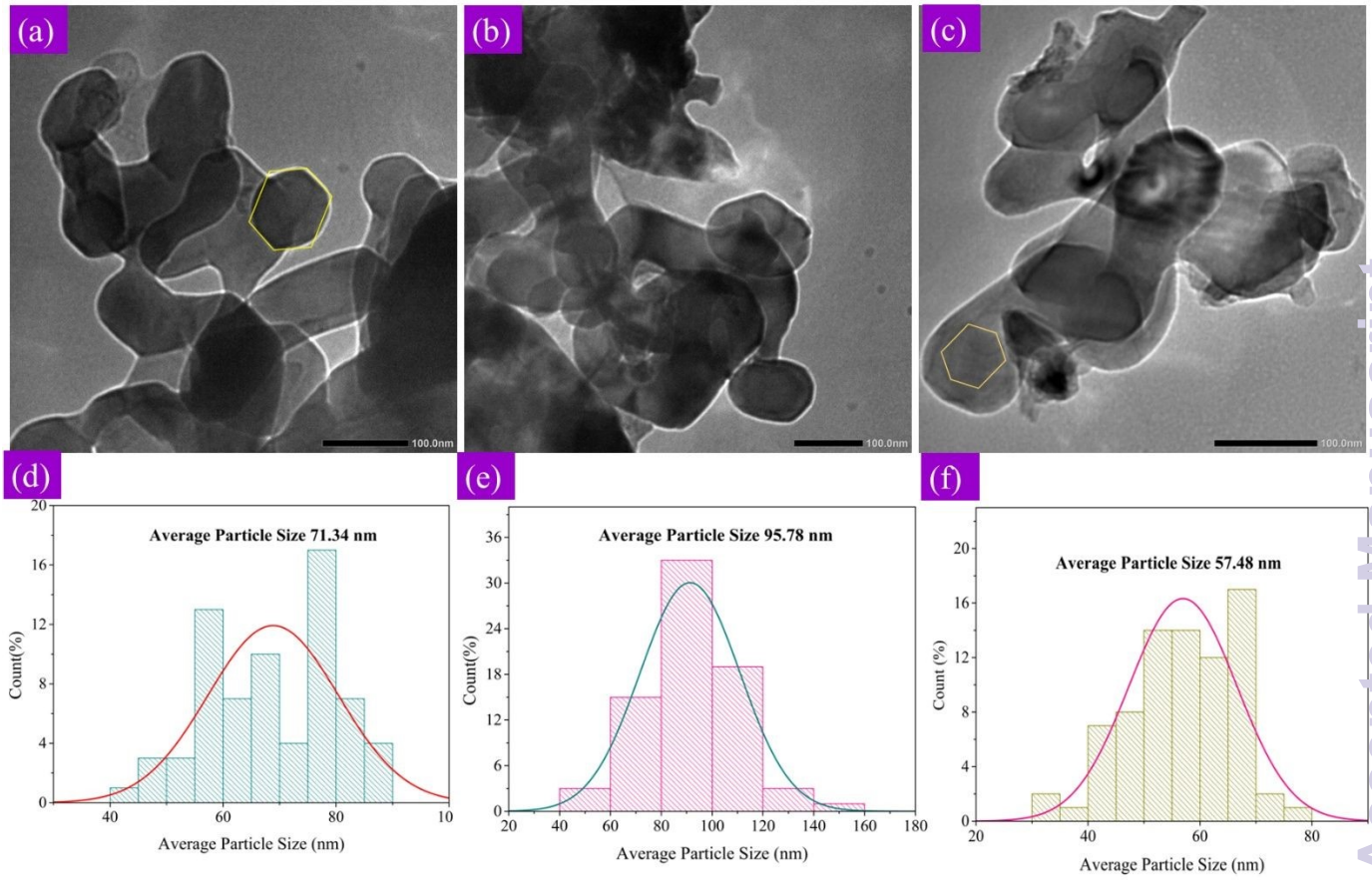

Fig. 10. Internal morphology analysis of α-alumina NPs.

The variation in particle size across samples reflects the influence of base selection during synthesis. Sample B, prepared with KOH, exhibited greater agglomeration and the largest average particle size, likely due to reduced nucleation efficiency and clustering effects. In contrast, sample A (NaOH) and sample C (NH_4OH) showed relatively uniform particle distributions and smaller average sizes, with the NH_4OH-derived sample exhibiting the lowest clustering degree. This interpretation is supported by its lower polydispersity index (PDI = 0.321) compared to the NaOH- and KOH-derived samples, indicating enhanced dispersion and surface reactivity. The particle size range obtained here aligns well with values reported in the literature [52], further validating our findings.

4.5.2 Energy Dispersive Spectroscopy (EDS) Pattern Analysis

View Article Online
DOI: 10.1039/D5MA01083G

Energy dispersive spectroscopy (EDS) facilitates microscale elemental analysis, allowing the identification of constituent elements and the detection of possible impurities within the sample [53]. **Fig. 11** represents the elemental profile of the synthesized α-alumina NPs through EDS analysis. Distinct peaks corresponding to aluminium, oxygen, and sodium were detected in sample A; aluminium, oxygen, and potassium in sample B; and only aluminium and oxygen in sample C, thereby confirming their respective elemental compositions. Additional signals of carbon and copper were observed, which originated from the carbon coated copper grid used to ensure electrical conductivity during the analysis.

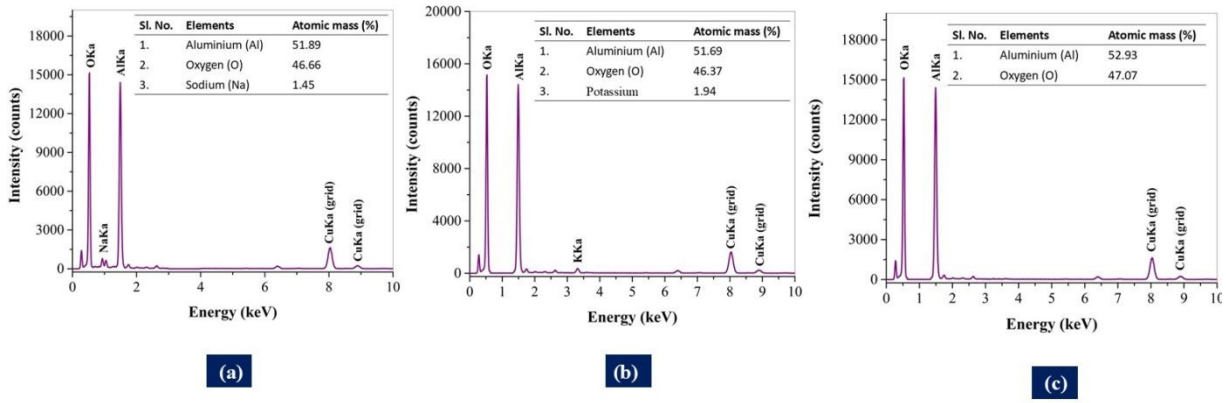

Fig. 11. EDS pattern of synthesized α-alumina NPs.

The EDS results for sample C revealed atomic mass percentages of aluminium (52.93%) and oxygen (47.07%), with no detectable impurities. The lack of additional elemental signals beyond aluminium and oxygen confirms the high purity of the synthesized α-alumina NPs. In sample A, the elemental composition was aluminium (51.89%), oxygen (46.66%), and sodium (1.45%), while in sample B, aluminium (51.69%), oxygen (46.37%), and potassium (1.94%) were identified. The synthesized α-alumina NPs exhibit complete purity, confirming their uniformity and phase purity in the sample.

5. Conclusion

This study demonstrates the significant influence of base selection on the co-precipitation synthesis of α-alumina NPs. Using aluminum nitrate as the precursor, three bases, NaOH, KOH,

View Article Online
DOI: 10.1039/D5MA01083G

and NH_4OH, were evaluated for their impact on crystallinity, morphology, and surface properties of the synthesized α-alumina NPs powders. Comprehensive analysis revealed that NH_4OH produced the smallest crystallite size (54.67 nm), the highest specific surface area (28.36 m^2/g), and complete phase purity, as confirmed by XRD and Rietveld refinement. In contrast, the KOH-based synthesis resulted in larger crystallites, lower surface area, and minor secondary phase formation. Multiple crystallite size determination models were applied to ensure accuracy and validate structural trends. UV–Vis spectroscopy indicated wide band gaps (5.4–5.5 eV) characteristic of α-alumina NPs, while DLS and zeta potential analyses confirmed better colloidal stability for NH_4OH and NaOH derived samples compared to KOH. The dominant (1 1 3) growth orientation was preserved across all samples. TGA-DSC analysis further revealed that NH_4OH-derived samples exhibited higher residual mass, indicating superior thermal stability, while all samples exhibited α-Al_2O_3 formation occurred between 1047-1121°C. TEM analysis of sample C (NH_4OH base) revealed uniformly distributed NPs with spherical morphology and minimal agglomeration. Particle size analysis confirmed the smallest average size (57.48 nm), consistent with XRD resuts. Samples A and B showed comparatively higher agglomeration and larger particle sizes. Overall, this work presents a detailed comparative approach to understanding how base type governs the structural and functional attributes of α-alumina NPs. This study was limited to NaOH, KOH, and NH_4OH, but future work should explore other bases, scale up the NH_4OH-assisted route for industrial feasibility, and evaluate the synthesized α-alumina nanoparticles in applications like ceramics, catalysis, and photocatalysis.

Acknowledgment

The author would like to express sincere gratitude to the Ministry of Science and Technology (MOST), Government of the People's Republic of Bangladesh authority for approval and technical support to enhance the R&D project “Synthesis of clay/alumina/Ag nanocomposite for the removal of textile dyes from aqueous system” (Ref no:39.00.0000.012.02.010.24-42 date: 04.03.2025). We sincerely express our gratitude to Dr. Samina Ahmed, Chairman of the Bangladesh Council of Scientific and Industrial Research (BCSIR), for granting permission and providing the necessary facilities to conduct this research.

View Article Online
DOI: 10.1039/D5MA01083G

References

[1] Li, H., Li, Y., Jiao, J., & Hu, H. M. (2011). Alpha-alumina nanoparticles induce efficient autophagy-dependent cross-presentation and potent antitumour response. *Nature nanotechnology*, *6*(10), 645-650. https://doi.org/10.1038/nnano.2011.153

[2] Park, Y. K., Tadd, E. H., Zubris, M., & Tannenbaum, R. (2005). Size-controlled synthesis of alumina nanoparticles from aluminum alkoxides. *Materials Research Bulletin*, *40*(9), 1506-1512. https://doi.org/10.1016/j.materresbull.2005.04.031

[3] Kaur, P., Khanna, A., Kaur, N., Nayar, P., & Chen, B. (2020). Synthesis and structural characterization of alumina nanoparticles. *Phase Transitions*, *93*(6), 596-605. https://doi.org/10.1080/01411594.2020.1765245

[4] Amirsalari, A., & Shayesteh, S. F. (2015). Effects of pH and calcination temperature on structural and optical properties of alumina nanoparticles. *Superlattices and microstructures*, *82*, 507-524. https://doi.org/10.1016/j.spmi.2015.01.044

[5] Kathirvel, P., Chandrasekaran, J., Manoharan, D., & Kumar, S. (2014). Preparation and characterization of alpha alumina nanoparticles by in-flight oxidation of flame synthesis. *Journal of alloys and compounds*, *590*, 341-345. https://doi.org/10.1016/j.jallcom.2013.12.105

[6] da Costa Cunha, G., Romão, L. P. C., & Macedo, Z. S. (2014). Production of alpha-alumina nanoparticles using aquatic humic substances. *Powder technology*, *254*, 344-351. https://doi.org/10.1016/j.powtec.2014.01.008

[7] Athari, S. S., Pourpak, Z., Folkerts, G., Garssen, J., Moin, M., Adcock, I. M., ... & Mortaz, E. (2016). Conjugated Alpha-Alumina nanoparticle with vasoactive intestinal peptide as a Nano-drug in the treatment of allergic asthma in mice. *European Journal of Pharmacology*, *791*, 811-820. https://doi.org/10.1016/j.ejphar.2016.10.014

[8] Ben-Nissan, B., Choi, A. H., & Cordingley, R. (2008). Alumina ceramics. In *Bioceramics and their clinical applications* (pp. 223-242). Woodhead Publishing. https://doi.org/10.1533/9781845694227.2.223

[9] Tavakoli, A. H., Maram, P. S., Widgeon, S. J., Rufner, J., Van Benthem, K., Ushakov, S., ... & Navrotsky, A. (2013). Amorphous alumina nanoparticles: structure, surface energy, and thermodynamic phase stability. *The Journal of Physical Chemistry C*, *117*(33), 17123-17130. https://doi.org/10.1021/jp405820g

View Article Online
DOI: 10.1039/D5MA01083G

[10] Mohamad, S. N. S., Mahmed, N., Halin, D. S. C., Razak, K. A., Norizan, M. N., & Mohamad, I. S. (2019, December). Synthesis of alumina nanoparticles by sol-gel method and their applications in the removal of copper ions (Cu2+) from the solution. In *IOP Conference Series: Materials Science and Engineering* (Vol. 701, No. 1, p. 012034). IOP Publishing. https://doi.org/10.1088/1757-899X/701/1/012034

[11] Lamouri, S., Hamidouche, M., Bouaouadja, N., Belhouchet, H., Garnier, V., Fantozzi, G., & Trelkat, J. F. (2017). Control of the γ-alumina to α-alumina phase transformation for an optimized alumina densification. *Boletín de la Sociedad Española de cerámica y vidrio*, *56*(2), 47-54. https://doi.org/10.1016/j.bsecv.2016.10.001

[12] Mirjalili, F., Hasmaliza, M., & Abdullah, L. C. (2010). Size-controlled synthesis of nano α-alumina particles through the sol–gel method. *Ceramics International*, *36*(4), 1253-1257. https://doi.org/10.1016/j.ceramint.2010.01.009

[13] Suchanek, W. L. (2010). Hydrothermal synthesis of alpha alumina (α-Al2O3) powders: study of the processing variables and growth mechanisms. *Journal of the American Ceramic Society*, *93*(2), 399-412. https://doi.org/10.1111/j.1551-2916.2009.03399.x

[14] Frikha, K., Limousy, L., Bouaziz, J., Bennici, S., Chaari, K., & Jeguirim, M. (2019). Elaboration of alumina-based materials by solution combustion synthesis: A review. *Comptes Rendus Chimie*, *22*(2-3), 206-219. https://doi.org/10.1016/j.crci.2018.10.004

[15] Alam, M. A., Ahmed, S., Sarkar, D., Bishwas, R. K., & Jahan, S. A. (2025). Preferred crystallographic design of monoclinic tenorite (CuO) nanocrystals by powder X-ray line diffraction. Chemistry of Inorganic Materials, 7, 100119. https://doi.org/10.1016/j.cinorg.2025.100119

[16] Rao, P. K., Jana, P., Ahmad, M. I., & Roy, P. K. (2019). Synthesis and characterization of zirconia toughened alumina ceramics prepared by co-precipitation method. *Ceramics International*, *45*(13), 16054-16061.https://doi.org/10.1016/j.ceramint.2019.05.121

[17] Rajaeiyan, A., & Bagheri-Mohagheghi, M. M. (2013). Comparison of sol-gel and co-precipitation methods on the structural properties and phase transformation of γ and α-

View Article Online
DOI: 10.1039/D5MA01083G

Al2O3 nanoparticles. *Advances in Manufacturing*, *1*(2), 176-182. https://doi.org/10.1007/s40436-013-0018-1

[18] Gholizadeh, Z., Aliannezhadi, M., Ghominejad, M., & Tehrani, F. S. (2023). High specific surface area γ-Al2O3 nanoparticles synthesized by facile and low-cost co-precipitation method. *Scientific Reports*, *13*(1), 6131. https://doi.org/10.1038/s41598-023-33266-0

[19] Jabbar, A., Abbas, A., Assad, N., Naeem-ul-Hassan, M., Alhazmi, H. A., Najmi, A., ... & Amin, H. M. (2023). A highly selective Hg 2+ colorimetric sensor and antimicrobial agent based on green synthesized silver nanoparticles using Equisetum diffusum extract. *RSC advances*, *13*(41), 28666-28675.

[20] Siddique, A. B., Amr, D., Abbas, A., Zohra, L., Irfan, M. I., Alhoshani, A., ... & Amin, H. M. (2024). Synthesis of hydroxyethylcellulose phthalate-modified silver nanoparticles and their multifunctional applications as an efficient antibacterial, photocatalytic and mercury-selective sensing agent. *International Journal of Biological Macromolecules*, *256*, 128009.

[21] Assad, N., Naeem-ul-Hassan, M., Ajaz Hussain, M., Abbas, A., Sher, M., Muhammad, G., ... & Farid-ul-Haq, M. (2025). Diffused sunlight assisted green synthesis of silver nanoparticles using Cotoneaster nummularia polar extract for antimicrobial and wound healing applications. *Natural Product Research*, *39*(8), 2203-2217.

[22] Muniz, F. T. L., Miranda, M. R., Morilla dos Santos, C., & Sasaki, J. M. (2016). The Scherrer equation and the dynamical theory of X-ray diffraction. *Foundations of Crystallography*, *72*(3), 385-390.

[23] Nasiri, S., Rabiei, M., Palevicius, A., Janusas, G., Vilkauskas, A., Nutalapati, V., & Monshi, A. (2023). Modified Scherrer equation to calculate crystal size by XRD with high accuracy, examples Fe2O3, TiO2 and V2O5. Nano Trends, 3, 100015.

[24] Aguilar-Marín, P., Angelats-Silva, L., Noriega-Diaz, E., Chavez-Bacilio, M., & Verde-Vera, R. (2020). Understanding the phenomenon of x-ray diffraction by crystals and related concepts. *European Journal of Physics*, *41*(4), 045501.

[25] Bishwas, R. K., Alam, M., & Jahan, S. A. (2025). Sustainable synthesis of nano-crystalline α-alumina from waste food packaging for efficient azithromycin removal.

View Article Online
DOI: 10.1039/D5MA01083G

Journal of Industrial and Engineering Chemistry. https://doi.org/10.1016/j.jiec.2025.07.027

[26] Alam, M. A., Bishwas, R. K., Mostofa, S., & Jahan, S. A. (2024). Crystallographic phase stability of nanocrystalline polymorphs TiO2 by tailoring hydrolysis pH. *South African Journal of Chemical Engineering*, *49*(1), 73-85.

[27] Bishwas, R. K., Alam, M. A., Sarkar, D., Mostofa, S., & Jahan, S. A. (2025). Crystallographic Phase Transformation of Nanocrystalline Ultrafine Alumina. *Journal of the Indian Chemical Society*, 102119.

[28] Alam, M. A., Shishir, M. K. H., Sarkar, D., Bishwas, R. K., & Jahan, S. A. (2025). X-ray line diffraction study of preferred oriented hexagonal zincite nanocrystals: A crystallographic investigation. *Journal of Crystal Growth*, 128230. https://doi.org/10.1016/j.jcrysgro.2025.128230

[29] Alam, M. A., Bishwas, R. K., Mostofa, S., & Jahan, S. A. (2024). Impact on preferred orientation and crystal strain behavior of nanocrystal anatase-TiO2 by X-ray diffraction technique. South African Journal of Chemical Engineering, 49, 348-352. https://doi.org/10.1016/j.sajce.2024.07.002

[30] Alam, M. A., Bishwas, R. K., Mostofa, S., Sarkar, D., & Jahan, S. A. (2024). X-ray crystallography derived diffraction properties of cuprite crystal as revealed by transmission electron microscopy. *Physics Open*, *20*, 100228.

[31] Bao, X., Wang, J., Wu, X., He, C., Luo, H., Bai, Q., ... & Zhao, S. (2023). The symmetry aspect of magnetocaloric effect in LaxBi0. 3-xCa0. 7MnO3 manganites. *Physica B: Condensed Matter*, *671*, 415410.

[32] Herzog, B., Schultheiss, A., & Giesinger, J. (2018). On the validity of Beer–Lambert law and its significance for sunscreens. *Photochemistry and photobiology*, *94*(2), 384-389.

[33] Khalid, Z., Ali, A., Siddique, A. B., Zaman, Y., Sibtain, M. F., Abbas, A., ... & Alwethaynani, M. S. (2025). Causonis trifolia-based green synthesis of multifunctional silver nanoparticles for dual sensing of mercury and ferric ions, photocatalysis, and biomedical applications. *RSC advances*, *15*(21), 16879-16893.

View Article Online
DOI: 10.1039/D5MA01083G

[34] Giannini, C., Ladisa, M., Altamura, D., Siliqi, D., Sibillano, T., & De Caro, L. (2016). X-ray diffraction: a powerful technique for the multiple-length-scale structural analysis of nanomaterials. *Crystals*, *6*(8), 87.

[35] Bishwas, R. K., Alam, M. A., & Jahan, S. A. (2025). Crystallographic and morphological characterization of high-crystalline α-alumina nanoparticles: A comprehensive X-ray diffraction and transmission electron microscopy study. *Chemical Physics Letters*, 142245.

[36] Alam, M. A., Sadia, S. I., Shishir, M. K. H., Bishwas, R. K., Ahmed, S., Al-Reza, S. M., & Jahan, S. A. (2025). Crystallinity integration and crystal growth behavior study of preferred oriented (111) cubic silver nanocrystal. Inorganic Chemistry Communications, 173, 113834. https://doi.org/10.1016/j.inoche.2024.113834

[37] Ahmed, S., Alam, M. A., Sadia, S. I., Bishwas, R. K., Hasanuzzaman, M., & Jahan, S. A. (2025). Stoichiometry low-temperature dynamics crystal growth interpret of zinc oxide hexagonal nanocrystals. *Next Materials*, *7*, 100636.

[38] Alam, M. A., Ahmed, S., Bishwas, R. K., Sarkar, D., & Jahan, S. A. (2025). Crystal growth behavior interpret of co-precipitated derived nickel oxide (NiO) nanocrystals. Nano-Structures & Nano-Objects, 42, 101494. https://doi.org/10.1016/j.nanoso.2025.101494

[39] Langford, J. I., Louër, D., & Scardi, P. (2000). Effect of a crystallite size distribution on X-ray diffraction line profiles and whole-powder-pattern fitting. *Applied Crystallography*, *33*(3), 964-974.

[40] Alam, M. A., Ahmed, S., Bishwas, R. K., Mostofa, S., & Jahan, S. A. (2025). X-ray crystallographic diffraction study by whole powder pattern fitting (WPPF) method: Refinement of crystalline nanostructure polymorphs TiO2. *South African Journal of Chemical Engineering*, *51*, 68-77. https://doi.org/10.1016/j.rinma.2025.100673

[41] Jbara, A. S., Othaman, Z., Aliabad, H. A., & Saeed, M. A. (2017). Electronic and Optical Properties of γ-and□-Alumina by First Principle Calculations. *Advanced Science, Engineering and Medicine*, *9*(4), 287-293.

[42] Santos, R. C. R., Longhinotti, E., Freire, V. N., Reimberg, R. B., & Caetano, E. W. S. (2015). Elucidating the high-k insulator α-Al2O3 direct/indirect energy band gap type through density functional theory computations. *Chemical Physics Letters*, *637*, 172-176.

View Article Online
DOI: 10.1039/D5MA01083G

[43] Ciraci, S., & Batra, I. P. (1983). Electronic structure of α-alumina and its defect states. *Physical Review B*, *28*(2), 982. https://doi.org/10.1103/PhysRevB.28.982

[44] Shah, R., Eldridge, D., Palombo, E., & Harding, I. (2014). Optimisation and stability assessment of solid lipid nanoparticles using particle size and zeta potential. *Journal of physical science*, *25*(1).

[45] Kanwal, M., Sher, M., Abbas, A., Akhtar, S., Siddique, A. B., ul Hasan, M. N., ... & Amin, H. M. (2025). Dual colorimetric sensing of Hg (II) and Fe (III) using sulfanilamide-stabilized silver nanoparticles and evaluating their photodegradation and antibacterial properties. *Journal of Water Process Engineering*, *75*, 107981

[46] Ullah, S., Khalid, R., Rehman, M. F., Irfan, M. I., Abbas, A., Alhoshani, A., ... & Amin, H. M. (2023). Biosynthesis of phyto-functionalized silver nanoparticles using olive fruit extract and evaluation of their antibacterial and antioxidant properties. *Frontiers in chemistry*, *11*, 1202252.

[47] Amin, S., Sher, M., Ali, A., Rehman, M. F., Hayat, A., Ikram, M., ... & Amin, H. M. (2022). Sulfonamide-functionalized silver nanoparticles as an analytical nanoprobe for selective Ni (II) sensing with synergistic antimicrobial activity. *Environmental Nanotechnology, Monitoring & Management*, *18*, 100735.

[48] Sun, D., Kang, S., Liu, C., Lu, Q., Cui, L., & Hu, B. (2016). Effect of zeta potential and particle size on the stability of SiO2 nanospheres as carrier for ultrasound imaging contrast agents. *International Journal of Electrochemical Science*, *11*(10), 8520-8529.

[49] Arami, H., Mazloumi, M., Khalifehzadeh, R., & Sadrnezhaad, S. K. (2008). Bundles of self-assembled boehmite nanostrips from a surfactant free hydrothermal route. *Journal of Alloys and Compounds*, *461*(1-2), 551-554.

[50] Mirjalili, F., Abdullah, L. C., Mohamad, H., Fakhru′ l-Razi, A., Dayang Radiah, A. B., & Aghababazadeh, R. (2011). Process for Producing Nano-Alpha-Alumina Powder. *International Scholarly Research Notices*, *2011*(1), 692594.

[51] Manuputty, M. Y., Lindberg, C. S., Botero, M. L., Akroyd, J., & Kraft, M. (2019). Detailed characterisation of TiO2 nano-aggregate morphology using TEM image analysis. *Journal of Aerosol Science*, *133*, 96-112.

View Article Online
DOI: 10.1039/D5MA01083G

[52] Ates, M., Demir, V., Arslan, Z., Daniels, J., Farah, I. O., & Bogatu, C. (2015). Evaluation of alpha and gamma aluminum oxide nanoparticle accumulation, toxicity, and depuration in Artemia salina larvae. *Environmental toxicology*, *30*(1), 109-118.

[53] Siddique, A. B., Shaheen, M. A., Abbas, A., Zaman, Y., Amin, H. M., Alam, M. M., ... & Ali, A. (2025). Sunlight-assisted greenly synthesised silver nanoparticles for highly selective mercury ion sensing, biomedical and photocatalytic applications. *International Journal of Environmental Analytical Chemistry*, 1-23.

View Article Online
DOI: 10.1039/D5MA01083G

Data Availability Statement

Data will be available on request.